AGU PUBLICATIONS

Water Resources Research

RESEARCH ARTICLE

10.1002/2015WR018427

Key Points:
- New permafrost thermal hydrology simulation capability is available in open-source parallel software
- The ATS software combines new surface and subsurface process representations in three dimensions
- Decadal projections of permafrost dynamics in a warming climate demonstrate the new capability

Supporting Information:
- Supporting Information S1

Correspondence to:
S. L. Painter,
paintersl@ornl.gov

Citation:
Painter, S. L., E. T. Coon, A. L. Atchley, M. Berndt, R. Garimella, J. D. Moulton, D. Svyatskiy, and C. J. Wilson (2016), Integrated surface/subsurface permafrost thermal hydrology: Model formulation and proof-of-concept simulations, *Water Resour. Res.*, *52*, doi:10.1002/2015WR018427.

Received 25 NOV 2015
Accepted 13 JUL 2016
Accepted article online 15 JUL 2016

© 2016. American Geophysical Union. All Rights Reserved.

Integrated surface/subsurface permafrost thermal hydrology: Model formulation and proof-of-concept simulations

Scott L. Painter[1], Ethan T. Coon[2], Adam L. Atchley[2], Markus Berndt[3], Rao Garimella[4], J. David Moulton[4], Daniil Svyatskiy[4], and Cathy J. Wilson[5]

[1]Climate Change Science Institute and Environmental Sciences Division, Oak Ridge National Laboratory, Oak Ridge, Tennessee, USA, [2]Computational Earth Sciences Group, Earth and Environmental Sciences Division, Los Alamos National Laboratory, Los Alamos, New Mexico, USA, [3]Computational Physics and Methods Group, Computer, Computational and Statistical Sciences Division, Los Alamos National Laboratory, Los Alamos, New Mexico, USA, [4]Applied Mathematics and Plasma Physics Group, Theoretical Division, Los Alamos National Laboratory, Los Alamos, New Mexico, USA, [5]Earth Systems Observations Group, Earth and Environmental Sciences Division, Los Alamos National Laboratory, Los Alamos, New Mexico, USA

Abstract The need to understand potential climate impacts and feedbacks in Arctic regions has prompted recent interest in modeling of permafrost dynamics in a warming climate. A new fine-scale integrated surface/subsurface thermal hydrology modeling capability is described and demonstrated in proof-of-concept simulations. The new modeling capability combines a surface energy balance model with recently developed three-dimensional subsurface thermal hydrology models and new models for nonisothermal surface water flows and snow distribution in the microtopography. Surface water flows are modeled using the diffusion wave equation extended to include energy transport and phase change of ponded water. Variation of snow depth in the microtopography, physically the result of wind scour, is modeled phenomenologically with a diffusion wave equation. The multiple surface and subsurface processes are implemented by leveraging highly parallel community software. Fully integrated thermal hydrology simulations on the tilted open book catchment, an important test case for integrated surface/subsurface flow modeling, are presented. Fine-scale 100 year projections of the integrated permafrost thermal hydrological system on an ice wedge polygon at Barrow Alaska in a warming climate are also presented. These simulations demonstrate the feasibility of microtopography-resolving, process-rich simulations as a tool to help understand possible future evolution of the carbon-rich Arctic tundra in a warming climate.

1. Introduction

Thawing of perennially frozen ground (permafrost) in a warming climate has the potential to both alter the hydrological regime [*Frampton et al.*, 2011; *Hinzman et al.*, 2013; *IPCC*, 2014; *Lyon et al.*, 2009; *Sjoberg et al.*, 2013; *Walvoord and Striegl*, 2007; *Walvoord et al.*, 2012] and induce significant feedback from the terrestrial system to the atmosphere [*Harden et al.*, 2012; *Hugelius et al.*, 2013; *McGuire et al.*, 2009; *Oechel et al.*, 1993; *Schaefer et al.*, 2011; *Tarnocai et al.*, 2009; *Wisser et al.*, 2011] through the resulting microbial decomposition and release of previously frozen organic carbon. Interest in understanding those potential impacts and feedbacks has prompted renewed interest in modeling permafrost dynamics in a warming climate (see recent review by *Kurylyk et al.* [2014]). Early modeling efforts [*Guymon and Luthin*, 1974; *Harlan*, 1973; *Jame and Norum*, 1980] were one-dimensional and focused on infrastructure vulnerability or general understanding of infiltration processes. More recent efforts [*Koven et al.*, 2013; *Lawrence et al.*, 2011; *Nicolsky et al.*, 2007; *Saito et al.*, 2007; *Sushama et al.*, 2007; *Takata et al.*, 2003] have focused on the land surface schemes in pan-Arctic or global applications, which necessarily require coarse spatial resolution and significant simplifications in the process representations. For example, those studies modeled heat and moisture movement in the vertical direction only, and are conceptually quite similar to the early modeling efforts. Three-dimensional computer codes with simplified representations of permafrost thermal hydrology have also been developed [*Bense et al.*, 2009; *McKenzie et al.*, 2007] to understand potential impacts of thawing on the hydrological cycle. See *Kurylyk et al.* [2014] for a recent review.

While reduced dimensionality and simplified representations of freeze/thaw dynamics in soils are appropriate for studies focusing on larger scales, more detailed models have an important role to play in building confidence in the approximations required for coarser scale models, as well as in exploring basic science questions about permafrost dynamics in a changing climate. For example, physically based representations of the partitioning among liquid, ice, and gas in freezing unsaturated soils are necessary to build confidence in models by establishing the clear link to laboratory experiments on freezing/thawing soils. Moreover, three-dimensional models are required for understanding the potential effects of microtopography on thaw response, energy exchange with the atmosphere, and greenhouse gas release. Questions about microtopography, lateral subsurface heat flows, and thermal erosion caused by overland flow are of particular interest for understanding carbon-rich polygonal tundra, because of the potential for organized trough networks to efficiently convey water across the tundra.

Kurylyk and Watanabe [2013] reviewed mathematical representations of freezing and thawing in variably saturated soils and recommended best practices for relating hydraulic conductivity and the soil water freezing curve to soil properties. Specifically, they recommend using soil water freezing curves and unsaturated hydraulic conductivity curves derived from soil moisture characteristic curves instead of empirical impedance factors and empirical soil freezing curves. Three-dimensional, variably saturated models with the level of process detail suggested by *Kurylyk and Watanabe* and capable of using unstructured computational meshes have recently been developed for use on single-core [*Painter*, 2011] and parallel [*Karra et al*., 2014]computer architectures.

Requirements for process-rich permafrost models go beyond the subsurface representations reviewed by *Kurylyk and Watanabe* [2013] and implemented previously by *Painter* [2011] and *Karra et al*. [2014]. Surface and subsurface flow systems are tightly coupled in permafrost regions because frozen ground is usually relatively impermeable, blocking infiltration. This coupling means that a comprehensive permafrost hydrology modeling capability requires representations of the surface flow system, surface energy balance, and effects of snow in addition to the subsurface thermal hydrology system [*Painter et al*., 2013].

Models that couple surface and subsurface thermal hydrology in 3-D have only recently started to appear. *Endrizzi et al*. [2014] couple 1-D subsurface energy balance with 3-D solutions to the Richards equation and overland flow representation in the GEOtop 2.0 model. They include a sophisticated treatment of snow thermal and surface energy balance processes.

Here we summarize implementation of a fully coupled permafrost thermal hydrology capability in highly parallel open source software called the Arctic Terrestrial Simulator (ATS). The capability is applicable to fine-scale simulations of permafrost-affected regions, which typically require 3-D solutions to the subsurface energy balance equations on unstructured meshes [*Painter et al*., 2013]. The surface energy balance and mass and energy conservation equations for the subsurface were described previously [*Karra et al*. 2014*; Painter and Karra*, 2014; *Atchley et al*., 2015]. Here the focus is on *integrated* surface/subsurface simulations of thermal hydrology in permafrost-affected regions. Specifically, the diffusion wave representation of surface flow is extended to include energy transport and phase change to represent the thermal aspects of overland flow; that surface flow representation is coupled to subsurface mass and energy conservation equations and to a surface energy balance. We also describe a phenomenological approach for distributing snow in the microtopography of lowland tundra landscapes. The intent is to provide a complete overview of the integrated surface/subsurface capability including descriptions of the process representations and process-coupling approaches, a high-level summary of numerical solution approaches, and proof-of-concept simulations of seasonal and decadal dynamics.

2. Overview of Thermal Hydrology in the Arctic Terrestrial Simulator

The Arctic Terrestrial Simulator (ATS) is not a standalone simulation tool. Instead it is a collection of permafrost-related process models and physics-based model couplers designed to work within a flexibly configured (composable) modeling system known as Amanzi-ATS. Amanzi-ATS is a derivative of the Amanzi

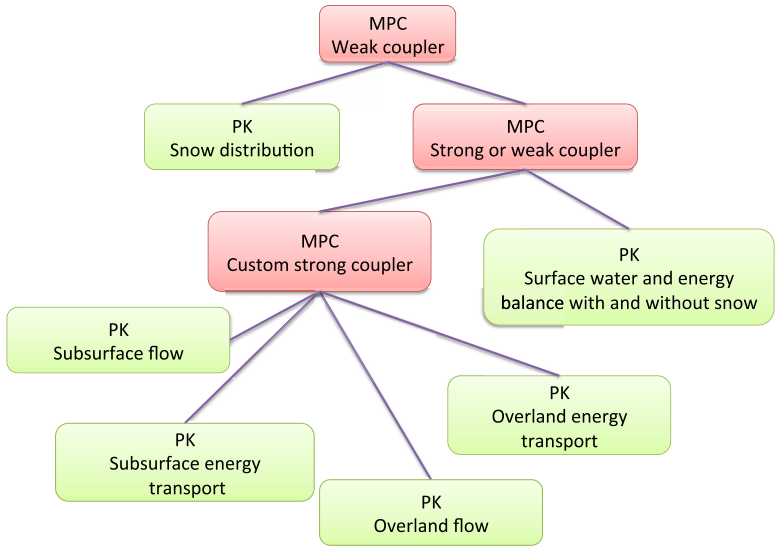

Figure 1. Model tree for fully integrated surface/subsurface thermal hydrology simulations with phase change. Here MPCs are multi-process coordinators and PKs are process kernels. Weak MPCs are sequential couplers (explicit coupling). Strong MPCs solve the coupled subsystem as one system of equations (implicit coupling). Custom strong couplers have been customized to incorporate physical understanding in preconditioners and extrapolation from the previous time step to establish an initial guess in the iterative solution process. The ability to customize the MPCs is a valuable feature of the Arcos framework [*Coon et al.*, 2016] that is exploited in ATS.

code [*Moulton et al.*, 2012] the result of combining Amanzi with a novel multiphysics process model management system known as Arcos [*Coon et al.*, 2016].

The ATS implements the modeling strategy outlined by *Painter et al.* [2013]. Specifically, ATS couples surface and subsurface thermal hydrology with a surface energy balance model, a single-layer model for snow thermal processes, and a model for snow distribution in the microtopography (Figure 1). In addition, simple models for the carbon cycle addressing soil organic matter decomposition and vegetation are included, but not addressed here. A dynamic mesh infrastructure is available and has been tested, but dynamic topography created by thaw subsidence is still under development and will be addressed in the future. The focus here is on integrated surface/subsurface thermal hydrology including surface energy balance and the effects of snow.

3. Subsurface Thermal Hydrology

Painter [2011] presented a two-component (air, water), three-phase (gas, liquid, ice) model for moisture dynamics in freezing, variably saturated porous media, and showed that the formulation is able to reproduce laboratory experiments on freezing soils. *Karra et al.* [2014] simplified that two-component formulation by treating the gas phase as passive in a Richards-type approximation, and showed that explicit representation of the air conservation equation is not necessary for Earth permafrost conditions, although it is clearly required for simulations of the Mars hydrology system [*Grimm and Painter*, 2009]. They also replace the model for partitioning among the ice, liquid, and gas phase used by Painter with a recently developed one [*Painter and Karra*, 2014] that provides a better representation of experimental results. The [*Karra et al.*, 2014] representation with the [*Painter and Karra*, 2014] partitioning model is used in ATS. Details and confidence-building comparisons to published experimental results may be found in those publications; here we provide a summary only.

In a Richards-type approximation with phase change, the conservation equation for water mass is

$$\frac{\partial}{\partial t}\left[\phi\left(\omega_g \eta_g s_g + \eta_l s_l + \eta_i s_i\right)\right] = -\nabla \cdot \left[\eta_l \mathbf{V}_l\right] + Q_w \tag{1}$$

where the Darcy velocity $\mathbf{V}_l$ is defined by

$$\mathbf{V}_l = -\frac{k_{rl}k}{\mu_l}(\nabla p_l + \rho_l g\hat{z}) \tag{2}$$

where the subscripts *l*, *g*, and *i* represent liquid, gas and ice phases, respectively.

Ice-phase air and dissolved air are ignored, so $\omega_i = 1$ and $\omega_l = 1$. Conservation of pore space requires $s_l + s_i + s_g = 1$. The vapor pressure in the pore space is assumed to be in equilibrium with the liquid phase above the freezing temperature and in equilibrium with the ice phase below freezing. Thus, $\omega_g p_g = p_{sat}(T)$ where p_{sat} is the saturated vapor pressure of water vapor over liquid or ice.

Equation (1) is valid for saturated or unsaturated conditions. Compressibility effects are incorporated through liquid compressibility and more importantly by allowing the porosity to depend on liquid pressure, which together are equivalent to use of a specific storage term.

Vapor diffusion is ignored in equation (1) and not used here, although it can easily be included [*Karra et al.*, 2014] and is available as an option in ATS.

The corresponding energy balance equation assumes local thermal equilibrium among the ice, liquid, gas and soil solids, leading to

$$\frac{\partial}{\partial t}\left[\phi \sum_{p=l,g,i}(\eta_p s_p u_p) + (1-\phi)C_{v,soil}T\right] = -\nabla\cdot(\eta_l h_l \mathbf{V}_l) + \nabla\cdot(\kappa_e \nabla T) + Q_E \tag{3}$$

Primary variables are temperature *T* and liquid pressure p_l. Note that no variable change is required when going from partially saturated to fully saturated conditions. However, the situation of full dryout $s_g = 1$ is not allowed.

Equilibrium relations between phase saturations and interphase capillary pressures introduce strong couplings between the energy and water conservation equations. In a gas-free soil, the Clapeyron equation provides a relationship between temperature and liquid-ice capillary pressure [e.g., *Williams and Smith*, 1989]

$$\rho_l L_f \frac{T - T_0}{T_0} = p_l - p_i \tag{5}$$

Here p_l and p_i are liquid and ice pressure, L_f is the heat of fusion for water ice, ρ_l is liquid density, *T* is temperature, and T_0 is the nominal freezing temperature.

The liquid saturation in this gas-free situation can then be related to the ice-liquid capillary pressure as

$$s_l = S_*(\beta(p_l - p_i)) \tag{6}$$

where S_* is the soil moisture retention curve for unfrozen conditions and β is unity for a colloidal soil and equal to the ratio of ice-liquid to liquid-air surface tensions for a noncolloidal soil [*Koopmans and Miller*, 1966]. Combining equations (5) and (6), the following is obtained

$$s_l = S_*(\beta \rho_l L_f \vartheta H(-\vartheta)) \tag{7}$$

where a dimensionless temperature $\vartheta = \frac{T - T_0}{T_0}$ has been defined and the Heaviside function $H(-)$ has been used to make equation (7) applicable to both frozen and unfrozen conditions.

Equation (7) relates the unfrozen water fraction to temperature and the soil moisture retention curve. Purely empirical approaches for representing unfrozen fraction to temperature are also available and have been extended to unsaturated conditions, but these empirical "freezing characteristic curves" must be developed anew for each soil type. By contrast, equation (7) uses the usual soil moisture retention curve in unfrozen conditions, which is relatively easy to obtain or estimate from information on soil texture.

Equation (7) is applicable to gas-free soil. *Painter and Karra* [2014] recently extended this relationship to soils with nonzero gas content and showed that the resulting model provides a reasonable representation of experimental data on phase partitioning below the freezing temperature. Two versions of the partitioning model are available, an implicit formulation that requires iteration to obtain the ice saturation given primary variables and a more approximate explicit equation that requires no iteration. Our experience with both

formulations suggests that the two formulations give nearly identical results except for tight clays. Thus, the explicit solution is used here:

$$s_l = \begin{cases} S_*(-\beta\rho_l L_f \vartheta) & \vartheta < \vartheta_f \\ S_*(p_g - p_l) & \vartheta \geq \vartheta_f \end{cases} \tag{8}$$

$$\vartheta_f \equiv -\frac{1}{\beta L_f \rho_l}\psi_*(1-s_g) \tag{9}$$

$$s_i = 1 - \frac{s_l}{S_*(p_g - p_l)} \tag{10}$$

Here $\psi_*(-)$ is the capillary pressure curve in unfrozen conditions. Equations (8) and (9) represent a truncation of the liquid water content at the total water content. That is, s_l is the smaller of $S_*(-\beta\rho_l L_f \vartheta)$ and the unfrozen result $S_*(p_g - p_l)$. Equations (8)–(10) are in the form convenient for numerical calculations. In a thermal Richards model that uses liquid pressure and temperature as primary variables, equation (8) can be solved for liquid saturation given the liquid pressure and temperature. The ice saturation is then obtained from equation (10), and the gas saturation from conservation of pore volume $s_g = 1 - s_l - s_i$

Several empirical forms exist for the soil moisture retention curve S_*. Van Genuchten's model [*Van Genuchten*, 1980] has been successful for a wide range of media, is widely used, and is adopted here. The remaining models for the dependence of the diffusion coefficients and thermal conductivity on temperature and soil parameters can be found in *Painter* [2011].

4. Thermal Surface Flow With Phase Change

Shallow overland flow is typically modeled with either the kinematic wave equation, which assumes that the overland flow rate is proportional to bed slope, or the diffusion wave equation, which assumes the overland flow rate is proportional to the gradient of water elevation. The kinematic wave approximation is often adequate for hillslopes but becomes problematic in flat terrain. In particular, the kinematic wave equation will not redistribute water on flat terrain and will thus maintain a nonphysical gradient in ponded depth on flat terrain. Because our interest is lowland tundra, which generally has very low relief, the more general diffusion wave equation is used here. In the variant of the diffusion wave approximation used in ATS, the surface water ponded depth δ_w is obtained from the solution of

$$\frac{\partial \delta_w}{\partial t} + \nabla \cdot (\delta_w \mathbf{U}_w) = q_w + \Gamma_{ex} \tag{11}$$

where δ_w is ponded depth [m], t is time [s], q_w is liquid precipitation/snow melt rate (m^3/m^2 s), Γ_{ex} is water exchange between surface and subsurface systems (m^3/m^2 s).

The surface flow velocity in ATS is

$$\mathbf{U}_w = -\frac{\delta_w^{2/3}}{n_{man}(\|\nabla Z_s\| + \varepsilon)^{1/2}} \nabla(Z_s + \delta_w) \tag{12}$$

where n_{man} is Manning's coefficient ($s/m^{1/3}$). The ponded depth and surface elevation Z_s are defined in two-dimension (x-y) and the vector operators are to be interpreted accordingly. Note also that the bed-slope is used in place of the gradient in water elevation in the denominator $\nabla(Z_s + \delta_w) \cong \nabla Z_s$ and we include a numerical parameter ε to regularize the velocity when the bed slope is zero. Equation (12) is a hybrid of the kinematic and diffusion wave equations that approximates the diffusion wave equation on sloping ground while providing physically reasonable results on flat ground (unlike the kinematic wave equation). This formulation gives similar results to other formulations of the kinematic and diffusion wave equation on benchmark problems, but converges faster than the full diffusion wave equation.

This formulation of overland flow does not represent energy transport, and does not allow for freezing of surface water. We add an energy balance equation including the advection of heat. The effects of freeze/thaw of surface water is included by introducing a liquid-ice partitioning factor (unfrozen fraction) χ, which depends on surface water temperature and varies from 0 to 1 as the temperature increases through the

freezing temperature. In addition, we switch from a conservation equation for water volume to a conservation equation for moles of water to allow for expansion of water substance upon freezing. The result is the following system:

$$\frac{\partial}{\partial t}[(\chi\eta_l+(1-\chi)\eta_i)\delta_w] + \nabla\cdot(\chi\eta_l\delta_w\mathbf{U}_w) = q_{rain}+q_{melt}-q_{evap}-q_{ss} \tag{13}$$

$$\mathbf{U}_w = -\frac{(\chi\delta_w)^{2/3}}{n_{man}(\|\nabla Z_s\|+\varepsilon)^{1/2}}\nabla(Z_s+\delta_w) \tag{14}$$

$$\begin{gathered}\frac{\partial}{\partial t}[(\chi\eta_l u_l+(1-\chi)\eta_i u_i)\delta_w] + \nabla\cdot(h_l\,\chi\eta_l\delta_w\mathbf{U}_w) - \\ \nabla\cdot[(\chi\kappa_l+(1-\chi)\kappa_i)\delta_w\nabla T_s] = q_E + h_{rain}q_{rain}+h_{melt}q_{melt} - h_l q_{evap} - h_{ss}q_{ss} - q_{Ess}\end{gathered} \tag{15}$$

This icy overland flow model reduces to the diffusion wave equation in unfrozen conditions. The phenomenological constitutive relationship $\chi(T)$ is a consequence of using a two-dimensional representation that neglects vertical variation in temperature within the shallow surface water. The unfrozen fraction is defined as a sigmoidal function (smoothed step function) with a user-specified width, typically take to be less than 1 K. Although details such as vertical stratification of ice/liquid are lost, mass and energy are conserved, heat is advected through moving surface water and transferred by conduction through water and ice, water is allowed to freeze and thaw depending on temperature, the enthalpy of phase change is accounted for in the difference between the internal energies, and the presence of ice reduces flow or blocks it completely. Thus, the most important features of overland flow in cold conditions are captured in a shallow-water approximation that can be coupled to the subsurface and surface energy balance.

Coupling between the surface and subsurface equations follow the boundary condition strategy of *Kollet and Maxwell* [2006], which enforces continuity of pressure and water flux to ensure mass conservation across the coupled system. A similar extension of that strategy is applied to the energy equation to enforce continuity of both temperature and energy fluxes. This method incorporates the surface equations as a nonlinear, Neumann-type boundary condition on the subsurface equations. No additional impedance coefficient is required when following this approach. The extension to the nonisothermal situation is straightforward with the only complication being how mobility (relative permeability) is defined for flows from surface to subsurface. In ATS, we use the unfrozen fraction for water on the surface $\chi(T)$ (see equations (13) and (14)). Thus water is free to infiltrate when surface temperatures are above the freezing temperature, but not when the surface water is frozen. Experience with this approach suggested one important tweak, which is implemented in ATS. Specifically, as the amount of surface water approaches 0 the relative permeability is forced to transition from $\chi(T)$ to 1. This allows very small quantities of ice to be advected into the subsurface and avoids the situation where many small time steps are required to allow a small quantity of surface ice to melt and infiltrate.

An example simulation is shown in Figure 2. This simulation is an extension of the "tilted open book" catchment, a common test problem for overland flow models [*Gaukroger and Werner*, 2011; *Panday and Huyakorn*, 2004]. The extension introduced here is to include an ice dam that is eroded away by warm water. The simulation starts with a slab of ice on an otherwise dry but cold surface. Warm rain is introduced to start the simulation. Initially the warm surface water pools behind the ice dam, but eventually the surface water overtops it and begins to thermally erode the ice. Eventually, all the ice has been melted and the simulation reverts to the standard open book configuration. There is no subsurface in this simulation. Integrated surface/subsurface simulations using this geometry are presented in section 7.

5. Surface Energy Balance and Snow

Details of the surface energy balance model in ATS are provided in *Atchley et al.* [2015, Appendix B]. A brief summary is provided here. The model is similar to surface energy balance models that are typically used in land surface models [*Hinzman et al.*, 1998; *Ling and Zhang*, 2004]. Specifically, the model balances incoming longwave and shortwave radiation, outgoing longwave radiation, sensible and latent heat transfer, and heat conduction through the snowpack to the underlying soil when snow is present (Figure 3), assuming the snow surface is in dynamic thermal equilibrium with its surroundings. Two important modifications to

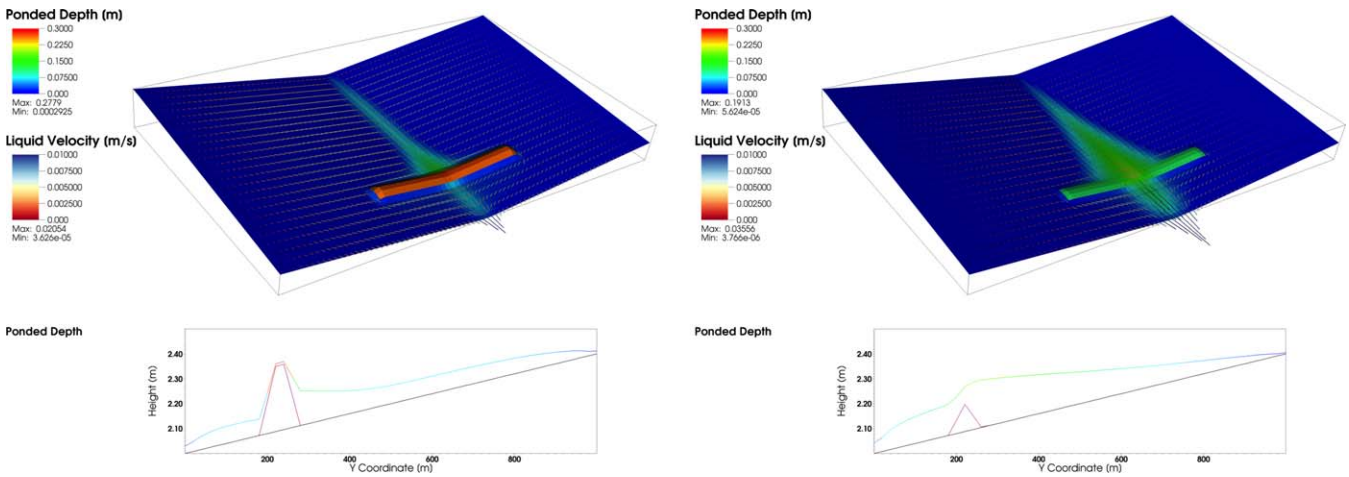

Figure 2. Results at two times for two-phase, nonisothermal overland flow simulation for the tilted open book configuration. The initial configuration has an ice dam, which is thermally eroded by surface flow as the simulation proceeds. Dimensions are 1 km by 1 km. The length of the arrows on the surface are proportional to the flow velocity. The bottom two plots are a cross section down the valley of the catchment. The lowermost line is the surface elevation and the top curve is water elevation. The intermediate curve (inverted V) is a representation of the ice dam. Although the ice dam is shown beneath the surface water, this representation is only for visualization purposes. The icy surface water model uses vertically averaged unfrozen fraction and does not represent ice/liquid stratification.

the standard formulation were implemented in ATS. First, a subgrid model is used to continuously transition between bare and snow-covered ground. This continuous transition between the two states of the surface is needed because ATS has options for a fully implicit time stepping that couples the surface energy balance with the surface flow component, which would fail to converge if the surface energy balance has abrupt transitions. The subgrid model is invoked when the snow height drops below a user-defined threshold (typically 2–5 cm). Within this transition region, the surface energy balance is calculated for both snow-covered and bare ground. A weighted average between the two results using snow depth to define the weights is then used to achieve the continuous transition. In addition to being robust for numerical calculation, the subgrid model is physically motivated by the observation that small amounts of snow will lie in discontinuous patches. The second modification from a standard snow model is that we use a single-layer model but retain some key features of multilayer models. Specifically we allow snow density to increase with snow age and include a thermally insulating depth hoar layer. The snow model is thus a compromise between multilayer and single-layer models and has been used with minimal calibration in 1-D models that successfully reproduce multiyear subsurface temperature measurements at Barrow Alaska [*Atchley et al.*, 2015; *Harp et al.*, 2016].

6. Snow Distribution

How snow precipitation is distributed on the landscape is an important question for distributed thermal hydrology simulators like ATS. At catchment to basin scales, orographic effects typically result in larger precipitation rates at higher elevations, and have been extensively studied. In addition, wind-driven snow-depth effects caused by preferential deposition, suspension, and saltation are important, especially in areas of heterogeneous vegetation and topography [*Pomeroy et al.*, 2006]. Models accounting for wind-driven effects fall into four general categories: physically based models [*Liston and Sturm*, 2002; *Pomeroy et al.*, 1993] that explicitly transport snow, statistical models that empirically correlate snow drifting to topographic structure and vegetation (see *Winstral et al.* [2013] for a recent example), hybrid physical/statistical methods [*Sturm and Wagner*, 2010], and phenomenological models [*Yi et al.*, 2014]. The latter class of models focuses on observable quantities rather than underlying mechanisms, but may go beyond purely statistical approaches by incorporating a limited set of process representations, often by analogy, to produce the target observable.

The high-level structure of integrated thermal hydrology simulations in ATS (see Figure 1) includes the option for a snow-distribution model that is sequentially (weakly) coupled to the other processes. The appropriate snow-distribution model is clearly application- and scale-dependent. The configurable nature

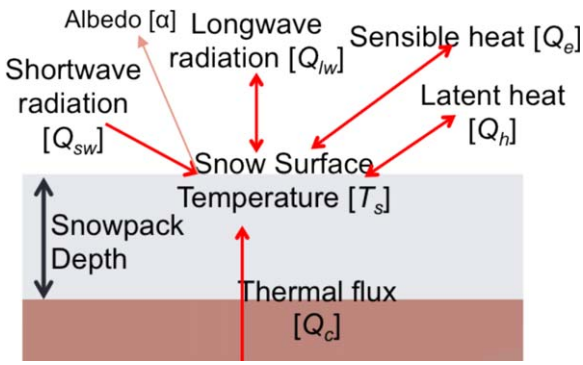

Figure 3. Surface energy balance schematic [*Atchley et al.*, 2015].

of ATS and the fact that the snow distribution model need not be strongly coupled to the other process representations makes it easy to substitute the appropriate snow distribution model, which for many applications will be statistical and site-specific.

The initial focus of ATS is on polygonal lowland tundra. Although of low relief generally, the microtopography associated with ice wedge polygons can significantly affect the snow depth at subpolygon scales. In particular, polygon rims typically have less snow than depressed regions of the microtopography (centers and troughs) because of wind scour [e.g., *Boike et al.*, 2013]. In addition, snow depth variations within a class of microtopographic features (e.g., within and among centers) are reported to be significantly smaller than variations between different microtopographic positions [*Boike et al.*, 2008; *Boike et al.*, 2013; *Gamon et al.*, 2012]. *Zhang et al.* [2012] model these effects phenomenologically by removing or adding a fixed fraction of the daily snowfall based on the geomorphic unit (center, rim, trough). *Yi et al.* [2014] note that the [*Zhang et al.*, 2012] approach overestimates snow depth. They impose a maximum snow elevation equal to 15 cm above polygon rims. The *Yi et al.* [2014] snow distribution model will track surface topography when there is little snow on the landscape, but transitions to a horizontal snow surface at specified height above the polygon rim when the total snowfall is above a user-specified threshold amount.

Here we use a phenomenological model for distributing incoming snow in the microtopography of polygonal tundra. Specifically, the diffusion wave equation is used to distribute snow precipitation across the landscape, filling in troughs and centers before rims. It is important to note that the diffusion wave equation is not intended to be a representation of the physics of snowfall in the near-surface atmosphere, but rather a convenient way to achieve the target phenomenon of having snow preferentially distributed into the low points of the landscape. The model includes a tunable parameter that controls how far a packet of falling snow may move. At each time step, the diffusion wave equation is used to distribute the incoming snow. That is, we evolve a diffusion wave equation over a pseudo-time step using the prior snow surface elevation as the surface (bed) elevation. To set the wave celerity, we specify a Manning's coefficient for the movement of this precipitated snow. The pseudo-time step and wave celerity define a characteristic scale that restricts the algorithm from moving snow too far on the landscape. Note that the pseudo-time step is independent of the physical time step. The pseudo-time step controls how far to advance the transient solution in the direction of the steady-state solution. Making it independent of the physical time step ensures that the distribution of snow does not change with decreasing physical time step, which is necessary for a solution that converges in time. This algorithm produces a horizontal snow surface when the amount of snow is sufficient to completely cover the highest points. Moreover, the algorithm provides control on how far snow can be moved in the distribution process, which we judge to be more realistic than, say, simply filling in the lowest elevations first. This allows the algorithm to be applicable in cases of small, yet nonzero, topographic gradients over scales of multiple polygons.

Specifically, at each time step we distribute incoming snow by calculating the *change* in snow depth given the snow depth in the previous time step and the surface topography. This is different from the approach of the overland flow model (section 4), which solves for ponded depth. To distribute snow, we solve between each physical time step a diffusion wave equation for the snow increment δ_{snow} (m) from time 0 to $\Delta\tau$, where $\Delta\tau$ is the pseudo-time step size. The initial condition for each solve is the uniform, nondistributed snow increment $r_s\Delta t$ where r_s is the snowfall rate (m/s), and Δt is the physical time step size.

$$\frac{\partial \delta_{snow}}{\partial t} + \nabla \cdot (\delta_{snow}\, \mathbf{U}_{snow}) = 0 \tag{16}$$

$$\mathbf{U}_{snow} = -\frac{\delta_{snow}^{2/3}}{n_s \|\nabla Z_{snow}\|^{1/2}} \nabla (Z_{snow} + \delta_{snow}) \tag{17}$$

Here Z_{snow} is the snow surface elevation (depth plus land-surface elevation) from the previous time step.

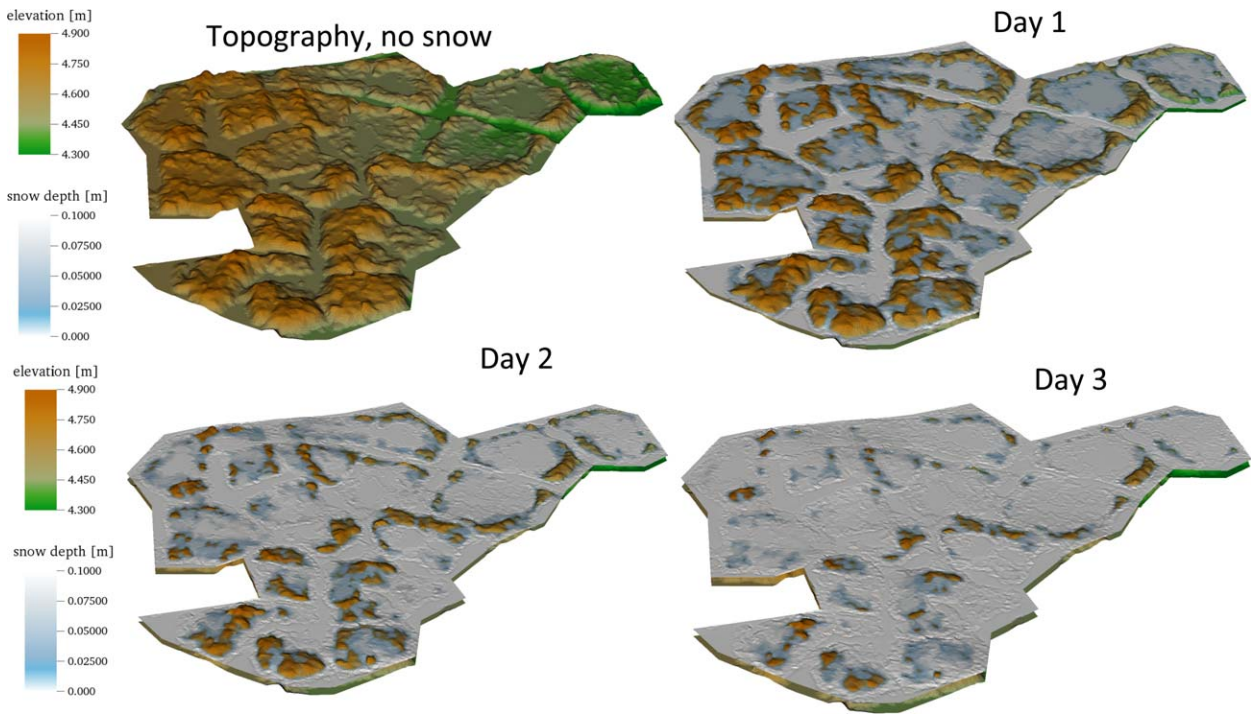

Figure 4. Illustrative simulation of snow distribution on fine-scale microtopography at the Barrow Environmental Observatory.

Snapshots in time for an example simulation using a lidar-derived digital elevation map of a small patch of the Barrow Environmental Observatory are shown in Figure 4. Although the model is simple and does not have a mechanistic basis in fluid dynamics and snow saltation/suspension physics, it provides reasonably realistic representation of the snow distribution. Early in the simulation when only a small amount of snow has fallen, the snow collects primarily in the low points (troughs and centers), simulating wind scouring off the rims. As more snow falls, larger fractions of the topography are covered in snow. Once enough snow has fallen, the snow level approaches horizontal, independent of the topography.

7. Solution Methods, Process Coupling, and Software Design

The Arctic Terrestrial Simulator is a collection of permafrost-related process models and physics-based model couplers in the Amanzi-ATS system. Amanzi-ATS uses the Trilinos [*Heroux et al*., 2003] framework for parallel infrastructure, an unstructured mesh framework [*Garimella et al*., 2014] for interacting with the computational mesh, and the Hypre library for algebraic multigrid preconditioners [*Falgout and Yang*, 2002]. Amanzi-ATS is the result of combining Amanzi with a novel multiphysics process model management system known as Arcos [*Coon et al*., 2016]. Arcos manages couplings among the various process models (denoted process kernels and abbreviated as PKs), which may be selected at runtime. That dynamic configuration is realized in Arcos through the use of two dynamically constructed directed graphs, one that arranges process couplings in a hierarchical manner, and one that specifies and manages dependencies among secondary variables that may be shared among multiple process kernels. Figure 1 is an example of the former. It is important to note that there are two types of objects within the graph, PKs and Multiprocess Coordinators (MPCs). A PK encapsulates the mathematical representation of a particular physical process or coupled set of processes, while the MPCs provide coupling among two or more PKs. An MPC may be regarded as a PK by MPCs at higher levels in the tree.

The interested reader is directed to *Moulton et al*. [2012] for details on the spatial discretization and nonlinear solution method in Amanzi, and by extension in ATS. Of note here is that fully unstructured general polyhedral meshes are supported, which provides great flexibility in representing subsurface structure. Dynamic mesh update capability, which is necessary to represent effects of differential thaw subsidence in ice-rich terrain, is available but has not been fully exercised. Discretization accuracy is maintained on the potentially

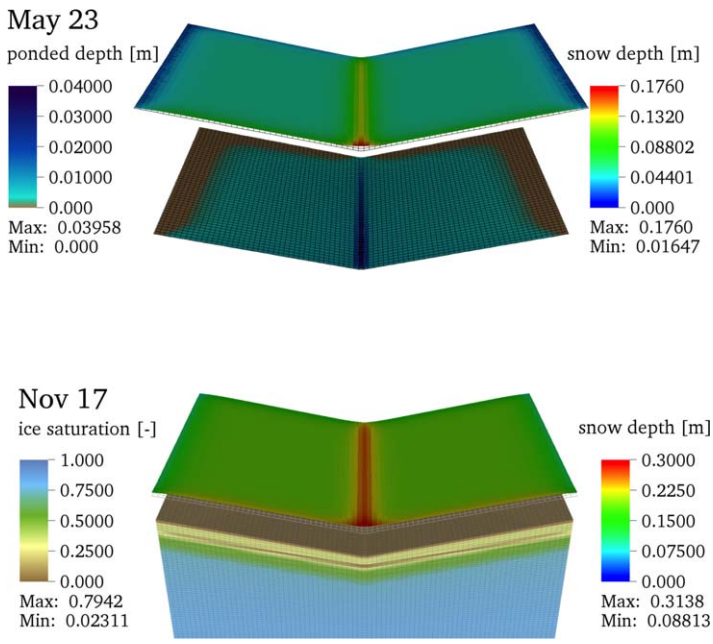

Figure 5. Results from integrated surface/subsurface thermal hydrology simulation on the open book (tilted-v) catchment. (bottom) Ice saturation index in the subsurface and snow depth on 17 November. (top) Snow depth and surface water depth during snowmelt (23 May). Horizontal dimensions are 1 km by 1 km. Vertical dimension is 10 m.

distorted grids through the use of the mimetic finite difference (MFD) method [*Beirao da Veiga*, 2014; *Lipnikov et al*., 2014]

In the MFD family of discretization schemes, the unknowns to be solved for include cell-centered quantities and face-centered quantities. That pressures defined on cell faces are in the set of unknowns in the MFD method is particularly convenient for coupling surface and subsurface. In particular, pressure continuity between the surface and subsurface systems is naturally enforced.

Time stepping in ATS is accomplished through the backward Euler method using a Nonlinear Krylov Acceleration (NKA) method [*Calef et al*., 2013; *Carlson and Miller*, 1998] to solve the resulting discretized residual equations using temperature and liquid pressures as primary variables. However, an important modification is made to the solution procedure to accommodate extreme nonlinearities associated with the liquid-ice phase change. Specifically, we use a heuristic to set the initial guess in the nonlinear iteration procedure. In that heuristic, the primary variables are projected forward from the previous time step to set the initial guess for cells that are not close to the phase transition. For cells that are close to the phase transition, we project in total energy and total water content and then back-solve for the corresponding pressure and temperature to start the iteration procedure. The projection in conserved quantities requires more computational effort, but makes a spurious update in the nonlinear solution method much less likely, resulting in a net gain in time-to-solution. These modifications will be described in detail in a future publication. The interested reader is referred to *Dall'Amico et al*. [2011] for alternative algorithmic adjustments to make the solution methods more robust near the freezing transition. A variable (adaptive) time-stepping strategy is employed in ATS where the next time step size is based on the number of nonlinear iterations at the previous time step.

8. Proof-of-Concept Simulations

Results of 2-D and 3-D fully integrated thermal hydrology simulations are presented in this section. As far as we are aware, these are the first simulations to couple all the processes described in sections 3–6 in fully multidimensional simulations.

8.1. Integrated Surface/Subsurface Hydrology on the Open Book Catchment

Results from the fully integrated thermal hydrology simulation on the open book domain are shown in Figure 5. These simulations were spun-up as described in the supporting information, then forced for 2 years using meteorological data from the Barrow Environmental Observatory. The bottom plot shows ice saturation index in the subsurface and snow depth on the surface on 17 November. The top plot shows snow depth and surface water depth during snowmelt at 23 May. The subsurface is fully frozen on 23 May and results for the subsurface are not shown. These snapshots illustrate some of the complexities in these integrated thermal hydrology simulations that would be missed with simpler models. On 23 May, much of the snow has melted and has disappeared completely from the highest parts of the catchment. Snowmelt has infiltrated the frozen ground and turned to ice, forming an ice-saturated layer that blocks further infiltration causing subsequent snowmelt to pond and run off into the central trough. During the late fall (Nov 17)

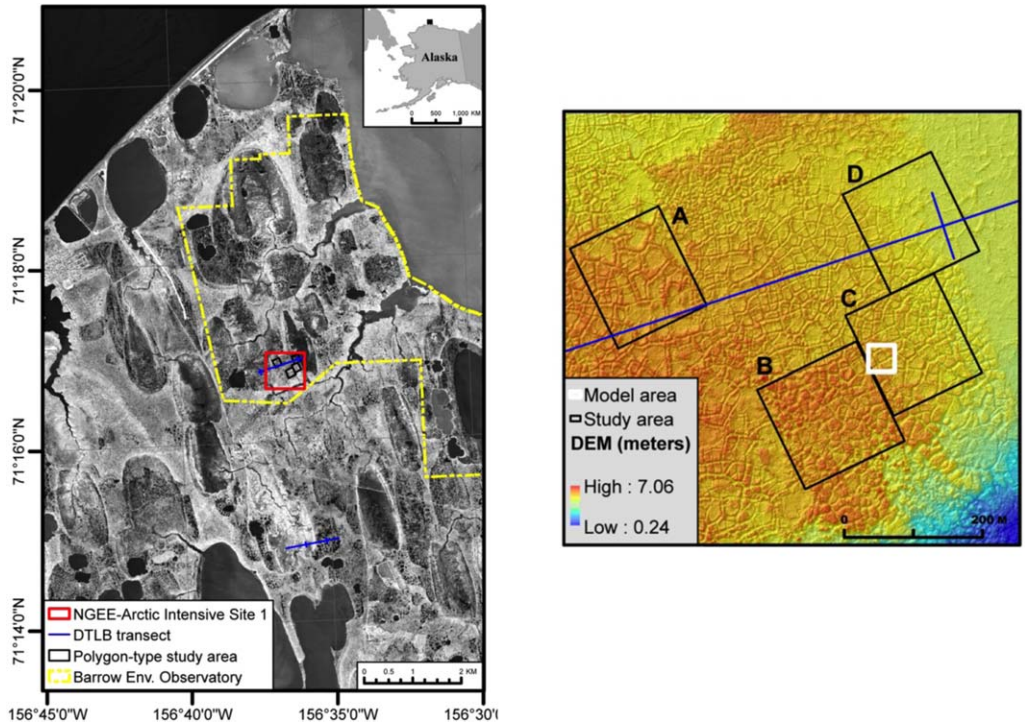

Figure 6. Location of study area used in permafrost thaw projections [*Atchley et al.*, 2015].

snow has fallen and collected preferentially in the low-lying area. The subsurface is almost all below freezing at this time, except for a thin unfrozen zone at about 0.5 meters depth.

8.2. Evolution of Permafrost at the Barrow Environmental Observatory

Here we show preliminary results for integrated surface/subsurface thermal hydrology of polygonal patterned ground at the Barrow Environmental Observatory in a projected future climate. The study location is shown in Figure 6. This example uses an unstructured mesh that follows a digital elevation map derived from lidar measurements processed to approximately 0.25 m resolution. The domain is a cross section across a low-centered ice-wedge polygon in study area C (see Figure 6). The mesh is a single slab of hexahedra that conforms to the surface topography and subsurface structure. The subsurface is assumed to be composed of moss, peat, and silt soil layers; moss is modeled as a porous medium with high porosity. This simulation was first spun-up as described in the supporting information. Earth system model projections for the site in the RCP8.5 scenario were then used to force the thermal hydrology simulation from 2006 to 2100. The climate forcings (air temperature, wind speed, humidity, incoming long- and short-wave radiation, and precipitation) were taken from the Community Earth System Model contribution to the Coupled Model Intercomparison Project. The air temperature projections for the site after applying a modest bias correction to match the long-term annual temperature of the site are shown in Figure 7. A similar bias correction was applied to the precipitation. The other climate variables were not adjusted. Lower boundary conditions are −6 C temperature and no mass flux. Boundary conditions on the left and right sides of the subsurface are specified as zero flux of energy and mass. These conditions presume the troughs (the boundaries

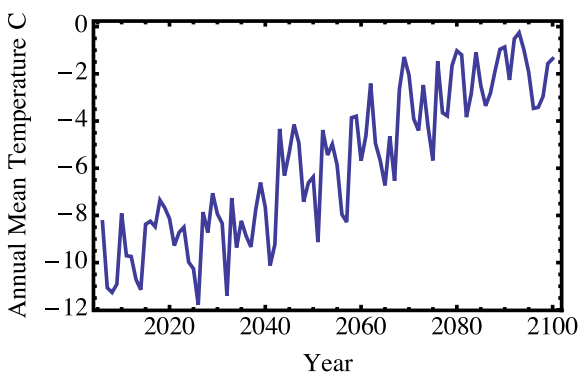

Figure 7. Annual mean temperatures used to drive the permafrost thaw projections.

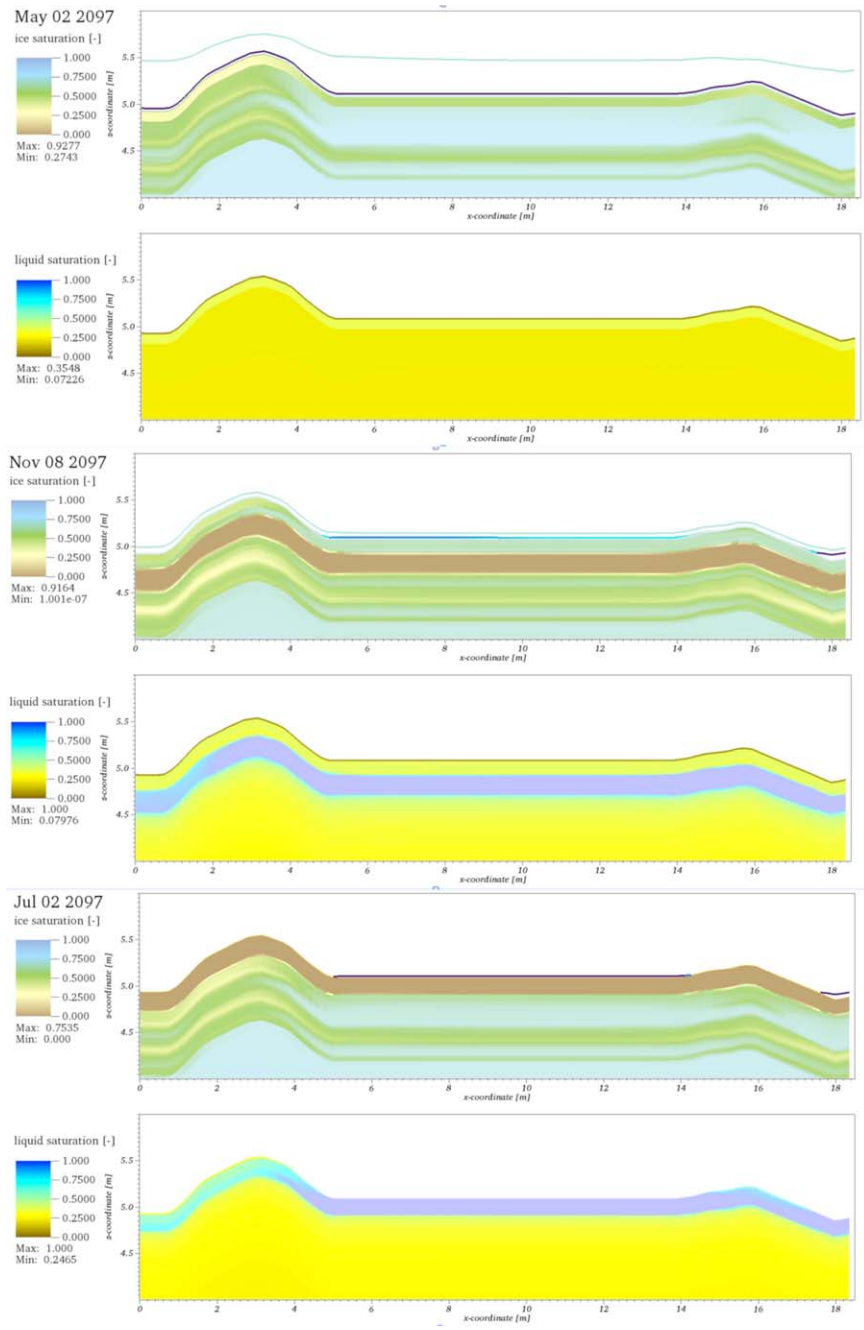

Figure 8. Results from permafrost thaw projections in year 2097. Shown are ice and liquid saturation indices at three times.

shown here) are natural symmetry points between neighboring polygons, which is a reasonable assumption as the troughs form natural symmetry boundaries. On the surface domain, the hydraulic boundary conditions are specified as a maximum ponded depth at the lowest point of the trough. This condition allows water to accumulate until the specified spill point is reached but then removes excess water above that. The physical motivation for this boundary condition is that water is blocked by a downstream obstruction out of the plane of the model domain until a spill point is reached, which is specified at 20 cm above the lowest trough elevation in these particular simulations. Lateral surface energy boundary conditions are no diffusive flux of energy, but advective heat transfer by outgoing water is allowed.

Three snapshots from the 2-D 100 year run are shown in Figure 8. The top plot at each time is a cross section showing ice saturation index. The bottom plot is liquid saturation index. The teal curve above the

landscape in the ice saturation plots is the elevation of the snow surface, while the darker curve that can be seen above the landscape is the elevation of (possibly frozen) ponded water. These snapshots illustrate some of the complexity of permafrost thermal hydrology systems that can be captured in an ATS simulation. The May 8 snapshot is during the snowmelt period. The thin layer of water above the landscape underneath the snow is caused by snowmelt that refroze upon hitting the frozen ground, temporarily clogging the pore space with ice and resulting in a thin layer of ponded water. The subsurface ice and water contents vary laterally. In particular, the center and right trough contain ponded water in the July and November snapshots, while the rims and left trough are dry. That the right trough contains water and the left trough does not is a consequence of the lower rim on the right, which allows water to flow laterally below the surface but above the thaw zone from the center to the right but not to the left. The banded structure of the ice content is a memory of previous years (2094 was the warmest in the particular realization of future climate used here, see Figure 7). It can be seen that the active layer has increased to about 1 meter by end of the century, compared to about 35 cm in the current climate.

9. Summary and Discussion

In the universe of hydrology simulations, the evolution of permafrost-affected regions in a warming climate is a particularly challenging application. The simulations summarized here are among the first to address fully coupled surface/subsurface permafrost thermal hydrology in multidimensional simulations. Our simulations extend those of *Endrizzi et al*. [2014] in that we include lateral transport of heat in the surface and subsurface on fully unstructured meshes in a parallel code. We demonstrated the core set of surface/subsurface thermal hydrology simulation capability identified in the modeling strategy of *Painter et al*. [2013]. These simulations address many of the key numerical challenges – nonlinear constitutive models, phase changes, robust coupling of several processes defined on different spatial domains, transitions among different states for the land surface, use of topography-following unstructured meshes – in a parallel community code. Key to achieving these simulations was careful attention to managing and incrementally increasing model complexity using a novel multiphysics management system [*Coon et al*., 2016].

ATS is a collection of physics modules and physics-informed model couplers for use in the Amanzi subsurface flow and transport simulation software. Amanzi has previously been shown to have good parallel scaling on complicated unstructured meshes. In polygonal Arctic tundra, potential sensitivities to fine-scale topography, which requires high spatial resolution, combined with the potential for long-range surface water flows, which requires large spatial domains, leads to large mesh sizes. The good parallel scaling of Amanzi and, by extension, ATS opens up the possibility of projecting permafrost response on climate-relevant domains while resolving small-scale topographic features.

Two numerical challenges remain and are clear targets for future research. First, convergence of the nonlinear system around the freeze/thaw transition has proved to be challenging, as has been reported elsewhere [*Dall'Amico et al*., 2011]. The algorithm introduced here for projecting in total water and energy content made 100 year runs possible on 2-D unstructured meshes, but further algorithmic improvements will be required to reach an acceptable time step to make large 3-D decadal projections feasible. Second, the representation of topography changes caused by the melting of massive subsurface ice requires mesh movement while maintaining water and energy balances inside the moving mesh cells.

The model used here for snow distribution on the landscape is phenomenological and tailored for distributing snow in microtopography associated with polygonal tundra. Although it provides results that appear realistic in this context, additional quantitative evaluations are warranted. Applications to permafrost-affected regions with heterogeneous vegetation and larger-scale variations in elevation will require site-specific distribution models.

Regardless of the remaining challenges, the simulations presented here demonstrate the feasibility of high-resolution integrated surface/subsurface permafrost hydrology simulations with many potential applications in understanding climate change impacts and feedbacks in the terrestrial Arctic.

Notation

s	phase saturation index.
p	pressure, Pa.
t	time, s.
ϕ	porosity.
η	molar density, mols/m^3.
ρ	mass density, kg/m^3.
ω	mole fraction of water substance.
k	absolute permeability, m^2.
k_r	relative permeability.
μ	dynamic viscosity, Pa-s.
$\hat{z}$	unit vector in the vertical direction.
g	acceleration due to gravity, m/s^2.
Q_w	mass source rate, kg/m^3-s.
T	temperature, K.
C_{vsoil}	volumetric heat capacity of the soil solid materials, J/m^3-K.
u	specific internal energy, J/mol.
h	specific enthalpy, J/mol.
κ_e	equivalent thermal conductivity for the soil-water-ice mixture, W/m-K.
Q_E	thermal energy source, W/m^3.
T_s	temperature of surface water, K.
$\chi=\chi(T_s)$	unfrozen fraction varies rapidly from 0 to 1 as temperature passes through 0 C.
κ_l	thermal conductivity of liquid water, W/m-K.
κ_i	thermal conductivity of water ice, W/m-K.
η_l	molar density of liquid, mol/m^3.
η_i	molar density of ice, mol/m^3.
h_l	specific enthalpy of liquid, J/mol.
h_{rain}	specific enthalpy of rain, J/mol.
h_{melt}	specific enthalpy of snowmelt, J/mol.
h_{ss}	specific enthalpy of surface-subsurface liquid flux, J/mol.
u_l	specific internal energy for liquid, J/mol.
u_i	specific internal energy for ice, J/m^3.
q_{rain}	water source delivered as rain, mol/m^2 –s.
q_{melt}	water source delivered as snowmelt, mol/m^2–s.
q_{evap}	water lost via evaporation, mol/m^2 –s.
q_{ss}	water lost to the subsurface, mol/m^2-s.
q_E	net rate of heat transfer to surface water from above via the surface energy balance excluding the convective component associated with incoming water, W/m^2.
q_{Ess}	heat transfer by conduction to subsurface, W/m^2.

Acknowledgments
This work was supported by the Los Alamos National Laboratory, Laboratory Direction Research and Development project LDRD201200068DR and by the Next Generation Ecosystem Experiment (NGEE-Arctic) project. NGEE-Arctic is supported by the Office of Biological and Environmental Research in the DOE Office of Science. We are also grateful to Nate Collier for careful review of the manuscript. We acknowledge the World Climate Research Programme's Working Group on Coupled Modelling, which is responsible for CMIP, and we thank the Community Earth System Modeling Contributors for producing and making available their model output. For CMIP the U.S. Department of Energy's Program for Climate Model Diagnosis and Intercomparison provides coordinating support and led development of software infrastructure in partnership with the Global Organization for Earth System Science Portals. The ATS software is open source and may be downloaded from https://github/amanzi/ats. Input and output files are available by contacting the authors at paintersl@ornl.gov.

References

Atchley, A. L., S. L. Painter, D. R. Harp, E. T. Coon, C. J. Wilson, A. K. Liljedahl, and V. E. Romanovsky (2015), Using field observations to inform thermal hydrology models of permafrost dynamics with ATS (v0.83), *Geosci. Model Dev.*, *8*(9), 2701–2722.

Beirao da Veiga, L., K. Lipnikov, and G. Manzini (2014), *The Mimetic Finite Difference Method for Elliptic Problems*, Springer, Switzerland.

Bense, V. F., G. Ferguson, and H. Kooi (2009), Evolution of shallow groundwater flow systems in areas of degrading permafrost, *Geophys. Res. Lett.*, *36*, L22401, doi:10.1029/2009GL039225.

Boike, J., C. Wille, and A. Abnizova (2008), Climatology and summer energy and water balance of polygonal tundra in the Lena River Delta, Siberia, *J. Geophys. Res.*, *113*, G03025, doi:10.1029/2007JG000540.

Boike, J., et al. (2013), Baseline characteristics of climate, permafrost and land cover from a new permafrost observatory in the Lena River Delta, Siberia (1998–2011), *Biogeosciences*, *10*(3), 2105–2128.

Calef, M. T., E. D. Fichtl, J. S. Warsa, M. Berndt, and N. N. Carlson (2013), Nonlinear Krylov acceleration applied to a discrete ordinates formulation of the k-eigenvalue problem, *J. Comput. Phys.*, *238*, 188–209.

Carlson, N., and K. Miller (1998), Design and application of a gradient-weighted moving finite element code I: In one dimension, *SIAM J. Sci. Comput.*, *19*(3), 728–765.

Coon, E. T., J. D. Moulton, and S. L. Painter (2016), Managing complexity in simulations of land surface and near-surface processes, *Environ. Modell. Software*, *78*, 134–149.

Dall'Amico, M., S. Endrizzi, S. Gruber, and R. Rigon (2011), A robust and energy-conserving model of freezing variably-saturated soil, *Cryosphere*, *5*(2), 469–484.

Endrizzi, S., S. Gruber, M. Dall'Amico, and R. Rigon (2014), GEOtop 2.0: Simulating the combined energy and water balance at and below the land surface accounting for soil freezing, snow cover and terrain effects, *Geosci. Model Dev.*, *7*(6), 2831–2857.
Falgout, R., and U. Yang (2002), hypre: A library of high performance preconditioners, in *Computational Science —ICCS 2002*, edited by P. A. Sloot et al., pp. 632–641, Springer, Berlin.
Frampton, A., S. Painter, S. W. Lyon, and G. Destouni (2011), Non-isothermal, three-phase simulations of near-surface flows in a model permafrost system under seasonal variability and climate change, *J. Hydrol.*, *403*(3-4), 352–359.
Gamon, J. A., G. P. Kershaw, S. Williamson, and D. S. Hik (2012), Microtopographic patterns in an arctic baydjarakh field: Do fine-grain patterns enforce landscape stability?, *Environ. Res. Lett.*, *7*(1), 015502.
Garimella, R. V., W. A. Perkins, M. W. Buksas, M. Berndt, K. Lipnikov, E. Coon, J. D. Moulton, and S. L. Painter (2014), Mesh infrastructure for coupled multiprocess geophysical simulations, *Procedia Eng.*, *82*, 34–45.
Gaukroger, A. M., and A. D. Werner (2011), On the Panday and Huyakorn surface–subsurface hydrology test case: Analysis of internal flow dynamics, *Hydrol. Processes*, *25*(13), 2085–2093.
Grimm, R. E., and S. L. Painter (2009), On the secular evolution of groundwater on Mars, *Geophys. Res. Lett.*, *36*, L24803, doi:10.1029/2009GL041018.
Guymon, G. L., and J. N. Luthin (1974), A coupled heat and moisture transport model for Arctic soils, *Water Resour. Res.*, *10*(5), 995–1001.
Harden, J. W., et al. (2012), Field information links permafrost carbon to physical vulnerabilities of thawing, *Geophys. Res. Lett.*, *39*, L15704, doi:10.1029/2012GL051958.
Harlan, R. L. (1973), Analysis of coupled heat-fluid transport in partially frozen soil, *Water Resour. Res.*, *9*(5), 1314–1323.
Harp, D. R., A. L. Atchley, S. L. Painter, E. T. Coon, C. J. Wilson, V. E. Romanovsky, and J. C. Rowland (2016), Effect of soil property uncertainties on permafrost thaw projections: A calibration-constrained analysis, *Cryosphere*, *10*(1), 341–358.
Heroux, M., et al. (2003), An Overview of Trilinos, *Tech. Rep. SAND2003-2927*, Sandia Natl. Lab., Albuquerque, N. M.
Hinzman, L. D., D. J. Goering, and D. L. Kane (1998), A distributed thermal model for calculating soil temperature profiles and depth of thaw in permafrost regions, *J. Geophys. Res.*, *103*(D22), 28,975–28,991.
Hinzman, L. D., C. J. Deal, A. D. McGuire, S. H. Mernild, I. V. Polyakov, and J. E. Walsh (2013), Trajectory of the Arctic as an integrated system, *Ecol. Appl.*, *23*(8), 1837–1868.
Hugelius, G., et al. (2013), A new data set for estimating organic carbon storage to 3 m depth in soils of the northern circumpolar permafrost region, *Earth Syst. Sci. Data*, *5*(2), 393–402.
IPCC (2014), Climate Change 2014: Synthesis report, in *Contribution of Working Groups I, II and III to the Fifth Assessment Report of the Intergovernmental Panel on Climate Change*, edited by R. K. Pachauri and L. A. Meyer, 151 pp., Geneva, Switzerland.
Jame, Y.-W., and D. I. Norum (1980), Heat and mass transfer in a freezing unsaturated porous medium, *Water Resour. Res.*, *16*(4), 811–819.
Karra, S., S. Painter, and P. Lichtner (2014), Three-phase numerical model for subsurface hydrology in permafrost-affected regions (PFLOTRAN-ICE v1. 0), *Cryosphere*, *8*(5), 1935–1950.
Kollet, S. J., and R. M. Maxwell (2006), Integrated surface–groundwater flow modeling: A free-surface overland flow boundary condition in a parallel groundwater flow model, *Adv. Water Resour.*, *29*(7), 945–958.
Koopmans, R. W. R., and R. D. Miller (1966), Soil freezing and soil water characteristic curves, *Soil Sci. Soc. Am. Proc.*, *30*(6), 680–685.
Koven, C. D., W. J. Riley, and A. Stern (2013), Analysis of permafrost thermal dynamics and response to climate change in the CMIP5 earth system models, *J Clim.*, *26*(6), 1877–1900.
Kurylyk, B. L., and K. Watanabe (2013), The mathematical representation of freezing and thawing processes in variably-saturated, non-deformable soils, *Adv. Water Resour.*, *60*, 160–177.
Kurylyk, B. L., K. T. B. MacQuarrie, and J. M. McKenzie (2014), Climate change impacts on groundwater and soil temperatures in cold and temperate regions: Implications, mathematical theory, and emerging simulation tools, *Earth Sci. Rev.*, *138*, 313–334.
Lawrence, D. M., A. G. Slater, and S. C. Swenson (2011), Simulation of present-day and future permafrost and seasonally frozen ground conditions in CCSM4, *J Clim.*, *25*(7), 2207–2225.
Ling, F., and T. Zhang (2004), A numerical model for surface energy balance and thermal regime of the active layer and permafrost containing unfrozen water, *Cold Reg. Sci. Technol.*, *38*(1), 1–15.
Lipnikov, K., G. Manzini, and M. Shashkov (2014), Mimetic finite difference method, *J. Comput. Phys.*, *257*, 1163–1227.
Liston, G. E., and M. Sturm (2002), Winter precipitation patterns in Arctic Alaska determined from a blowing-snow model and snow-depth observations, *J. Hydrometeorol.*, *3*(6), 646–659.
Lyon, S. W., G. Destouni, R. Giesler, C. Humborg, M. Morth, J. Seibert, J. Karlsson, and P. A. Troch (2009), Estimation of permafrost thawing rates in a sub-arctic catchment using recession flow analysis, *Hydrol. Earth Syst. Sci.*, *13*(5), 595–604.
McGuire, A. D., L. G. Anderson, T. R. Christensen, S. Dallimore, L. Guo, D. J. Hayes, M. Heimann, T. D. Lorenson, R. W. Macdonald, and N. Roulet (2009), Sensitivity of the carbon cycle in the Arctic to climate change, *Ecol. Monogr.*, *79*(4), 523–555.
McKenzie, J. M., C. I. Voss, and D. I. Siegel (2007), Groundwater flow with energy transport and water–ice phase change: Numerical simulations, benchmarks, and application to freezing in peat bogs, *Adv. Water Resour.*, *30*(4), 966–983.
Moulton, J. D., M. Berndt, R. Garimella, L. Prichett-Sheats, G. Hammond, M. Day, and J. C. Meza (2012), High-level design of Amanzi, the multi-process high performance computing simulator, *ASCEM-HPC-2011-03-1*, Off. of Environ. Manage., U. S. Dep. of Energy, Washington, D. C.
Nicolsky, D. J., V. E. Romanovsky, V. A. Alexeev, and D. M. Lawrence (2007), Improved modeling of permafrost dynamics in a GCM land-surface scheme, *Geophys. Res. Lett.*, *34*, L08501, doi:10.1029/2007GL029525.
Oechel, W. C., S. J. Hastings, G. Vourlitis, M. Jenkins, G. Riechers, and N. Grulke (1993), Recent change of Arctic Tundra ecosystems from a net carbon-dioxide sink to a source, *Nature*, *361*(6412), 520–523.
Painter, S. L. (2011), Three-phase numerical model of water migration in partially frozen geological media: Model formulation, validation, and applications, *Comput. Geosci.*, *15*(1), 69–85.
Painter, S. L., and S. Karra (2014), Constitutive model for unfrozen water content in subfreezing unsaturated soils, *Vadose Zone J.*, *13*(4).
Painter, S. L., J. D. Moulton, and C. J. Wilson (2013), Modeling challenges for predicting hydrologic response to degrading permafrost, *Hydrogeol. J.*, *21*(1), 221–224.
Panday, S., and P. S. Huyakorn (2004), A fully coupled physically-based spatially-distributed model for evaluating surface/subsurface flow, *Adv. Water Resour.*, *27*(4), 361–382.
Pomeroy, J. W., D. M. Gray, and P. G. Landine (1993), The Prairie Blowing Snow Model: Characteristics, validation, operation, *J. Hydrol.*, *144*(1), 165–192.
Pomeroy, J. W., D. S. Bewley, R. L. H. Essery, N. R. Hedstrom, T. Link, R. J. Granger, J. E. Sicart, C. R. Ellis, and J. R. Janowicz (2006), Shrub tundra snowmelt, *Hydrol. Processes*, *20*(4), 923–941.

Saito, K., M. Kimoto, T. Zhang, K. Takata, and S. Emori (2007), Evaluating a high-resolution climate model: Simulated hydrothermal regimes in frozen ground regions and their change under the global warming scenario, *J. Geophys. Res.*, *112*, F02S11, doi:10.1029/2006JF000577.

Schaefer, K., T. J. Zhang, L. Bruhwiler, and A. P. Barrett (2011), Amount and timing of permafrost carbon release in response to climate warming, *Tellus, Ser. B*, *63*(2), 165–180.

Sjoberg, Y., A. Frampton, and S. W. Lyon (2013), Using streamflow characteristics to explore permafrost thawing in northern Swedish catchments, *Hydrogeol. J.*, *21*(1), 121–131.

Sturm, M., and A. M. Wagner (2010), Using repeated patterns in snow distribution modeling: An Arctic example, *Water Resour. Res.*, *46*, W12549, doi:10.1029/2010WR009434.

Sushama, L., R. Laprise, D. Caya, D. Verseghy, and M. Allard (2007), An RCM projection of soil thermal and moisture regimes for North American permafrost zones, *Geophys. Res. Lett.*, *34*, L20711, doi:10.1029/2007GL031385.

Takata, K., S. Emori, and T. Watanabe (2003), Development of the minimal advanced treatments of surface interaction and runoff, *Global Planet. Change*, *38*(1), 209–222.

Tarnocai, C., J. G. Canadell, E. A. G. Schuur, P. Kuhry, G. Mazhitova, and S. Zimov (2009), Soil organic carbon pools in the northern circumpolar permafrost region, *Global Biogeochem. Cycles*, *23*, GB2023, doi:10.1029/2008GB003327.

Van Genuchten, M. T. (1980), A closed-form equation for predicting the hydraulic conductivity of unsaturated soils, *Soil Sci. Soc. Am. J.*, *44*(5), 892–898.

Walvoord, M. A., and R. G. Striegl (2007), Increased groundwater to stream discharge from permafrost thawing in the Yukon River basin: Potential impacts on lateral export of carbon and nitrogen, *Geophys. Res. Lett.*, *34*, L12402, doi:10.1029/2007GL030216.

Walvoord, M. A., C. I. Voss, and T. P. Wellman (2012), Influence of permafrost distribution on groundwater flow in the context of climate-driven permafrost thaw: Example from Yukon Flats Basin, Alaska, United States, *Water Resour. Res.*, *48*, W07524, doi:10.1029/2011WR011595.

Williams, P. J., and M. W. Smith (1989), *The Frozen Earth. Fundamentals of Geocryology*, 306 pp., Cambridge Univ. Press, Cambridge, U. K.

Winstral, A., D. Marks, and R. Gurney (2013), Simulating wind-affected snow accumulations at catchment to basin scales, *Adv. Water Resour.*, *55*, 64–79.

Wisser, D., S. Marchenko, J. Talbot, C. Treat, and S. Frolking (2011), Soil temperature response to 21st century global warming: The role of and some implications for peat carbon in thawing permafrost soils in North America, *Earth Syst. Dyn.*, *2*(1), 121–138.

Yi, S., K. Wischnewski, M. Langer, S. Muster, and J. Boike (2014), Freeze/thaw processes in complex permafrost landscapes of northern Siberia simulated using the TEM ecosystem model: Impact of thermokarst ponds and lakes, *Geosci. Model Dev.*, *7*(4), 1671–1689.

Zhang, Y., T. Sachs, C. Li, and J. Boike (2012), Upscaling methane fluxes from closed chambers to eddy covariance based on a permafrost biogeochemistry integrated model, *Global Change Biol.*, *18*(4), 1428–1440.